JOURNAL OF SYNCHROTRON RADIATION

ISSN 1600-5775

Received 16 September 2015
Accepted 24 March 2016

Edited by G. E. Ice, Oak Ridge National Laboratory, USA

Keywords: sapphire Fabry–Perot resonator; coherent X-rays; backward diffraction; dynamical diffraction; high-resolution monochromator.

Sapphire hard X-ray Fabry–Perot resonators for synchrotron experiments

Yi-Wei Tsai,[a,b] Yu-Hsin Wu,[a] Ying-Yi Chang,[b] Wen-Chung Liu,[a] Hong-Lin Liu,[a] Chia-Hong Chu,[b] Pei-Chi Chen,[c] Pao-Te Lin,[c] Chien-Chung Fu[c] and Shih-Lin Chang[a,b]*

[a]Department of Physics, National Tsing Hua University, Hsinchu 300, Taiwan, [b]National Synchrotron Radiation Research Center, Hsinchu 300, Taiwan, and [c]Institute of NanoEngineering and MicroSystems, National Tsing Hua University, Hsinchu 300, Taiwan. *Correspondence e-mail: slchang@phys.nthu.edu.tw

Hard X-ray Fabry–Perot resonators (FPRs) made from sapphire crystals were constructed and characterized. The FPRs consisted of two crystal plates, part of a monolithic crystal structure of Al_2O_3, acting as a pair of mirrors, for the backward reflection (0 0 0 30) of hard X-rays at 14.3147 keV. The dimensional accuracy during manufacturing and the defect density in the crystal in relation to the resonance efficiency of sapphire FPRs were analyzed from a theoretical standpoint based on X-ray cavity resonance and measurements using scanning electron microscopic and X-ray topographic techniques for crystal defects. Well defined resonance spectra of sapphire FPRs were successfully obtained, and were comparable with the theoretical predictions.

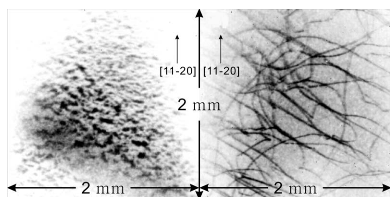

© 2016 International Union of Crystallography

1. Introduction

X-ray optical components, such as monochromators, beam splitters, analyzers, phase plates, resonators, *etc.*, are frequently employed in synchrotron beamlines to shape the beam properties for specific experiments. With the demonstration of Fabry–Perot resonators (FPRs) of silicon for hard X-rays (Chang *et al.*, 2005), in principle, the cavity resonance can improve the beam coherence and energy resolution, which are the essential parameters affecting the quality of scattering/diffraction and imaging. The hard X-ray FPR usually consists of crystal plates as reflective planes, and the incident beam is reflected back and forth between the two crystals *via* backward Bragg diffraction, thus generating cavity resonance. Recently, novel hard X-ray resonant devices based on silicon for synchrotron experiments have been reported, including curved multi-plate crystal resonators (Chang *et al.*, 2010) for simultaneous beam focusing and cavity resonance, ultrahigh-efficiency and -resolution inclined-incidence resonators (Wu *et al.*, 2015), and single-mode hard X-ray resonators (Tsai *et al.*, 2015), which demonstrate the potential and the possibilities of silicon hard X-ray FPRs. The use of silicon crystals has advantages such as an approximately dislocation-free crystal quality (Dash, 1959), well understood properties and well established micro-structure fabrication techniques.

However, silicon is not the most ideal material for hard X-ray FPRs. In the case of a silicon FPR at 14.4388 keV, whenever the backward diffraction Si(12 4 0) takes place, the 24-beam multiple diffraction effect (Sutter *et al.*, 2001) ensues because of the high symmetry of the diamond structure in silicon. The coexistence of 24 beams decreases the reflectivity of the backward diffraction, thus lowering the efficiency of the resonator (Shvyd'ko & Gerdau, 1999). Also, silicon has

a slightly higher absorption coefficient for hard X-rays than other proposed FPR materials such as diamond (Shvyd'ko *et al.*, 2011) and sapphire (Chena *et al.*, 2003). Moreover, the X-ray reflectivity of sapphire is higher, because of the larger Debye–Waller factor (Shvyd'ko & Gerdau, 1999; Shvyd'ko *et al.*, 2003), and the storage of X-ray photons of sapphire interferometers has been observed from time-resolved transmission measurements (Shvyd'ko *et al.*, 2003).

In this paper we focus on sapphire hard X-ray FPRs for synchrotron experiments and demonstrate the detection of cavity resonance spectra. Sapphire crystals are chosen with an orientation for a simple back reflection to achieve resonance without accompanied multiple diffractions. This feature could improve the reflectivity of the crystal and enhance the cavity resonance efficiency. In the following, we will describe the selection of high-quality sapphire crystals, fabrication of sapphire FPRs, and synchrotron diffraction experiments.

2. Experimental setup

2.1. Selection of high-quality sapphire crystals

Two kinds of sapphire wafers are inspected: one grown by the Kyropoulos method (KYM) and the other optical grade sapphire grown by the heat exchanger method (HEM) (Khattak & Schmid, 2001). The crystal quality of these two kinds of sapphire wafers was verified using X-ray topography and the dislocation densities were measured. All the sapphire crystals were *c*-axis wafers with the orientation along [0001].

Topographic experiments were carried out at the In-achromatic Superconducting Wiggler beamline 07A at the National Synchrotron Radiation Research Center (NSRRC), Taiwan. An X-ray photon energy of 19 keV was employed to lower the effects of crystal absorption. In order to increase the detecting area and the spatial resolution in topography, a silicon wafer with (001) orientation was used, after a Si(111) double-crystal monochromator (DCM), as a beam collimator (Fig. 1). The collimator employed the asymmetry diffraction Si(115) to extend the vertical beam size from 0.23 mm to 6.71 mm and to compress the vertical beam divergence from 0.32 mrad to 0.06 mrad. The collimated beam impinged on a sapphire wafer in Laue diffraction geometry. A CCD detector was employed to record the topographic images. Figs. 2(*a*) and 2(*b*) show topographs of a KYM sapphire wafer and a HEM sapphire wafer, respectively, which were obtained with $Al_2O_3(1 1 \bar{2} 0)$ Laue diffraction. From the topographic images the dislocation density was estimated to be around 1600 cm^{-2} for the HEM wafers; the dislocation density of the KYM wafers was too high to be quantified.

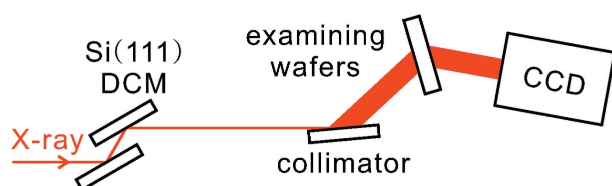

Figure 1
Schematic representation of a collimator for topographic experiments.

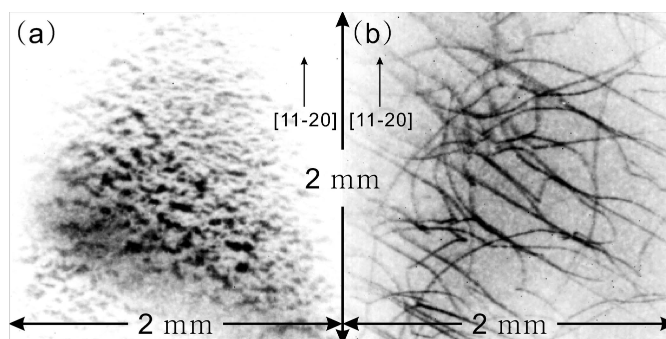

Figure 2
Topographic images of (*a*) the sapphire wafer grown using the Kyropoulos method (crystal thickness 0.423 mm) and (*b*) the optical grade sapphire wafer grown using the heat exchanger method (crystal thickness 1.0 mm).

From the topographic investigation, we chose the HEM optical grade sapphire crystals for making X-ray resonators, as the dislocation density was the lowest (below 10^5 cm^{-2}) among the two available crystals. The X-ray resonator of KYM was also used for comparison.

2.2. Fabrication of sapphire FPRs

Usually the simplest form of an X-ray FPR consists of two parallel crystal plates with thicknesses T_1 and T_2 separated by a gap d_g. Utilizing a backward diffraction of the crystal plates, whose reciprocal lattice vector is normal to the surface of the crystal plates, the incident beam is reflected back and forth in between the gap, thus generating successively reflected backward and forward beams which are interfering with each other. Therefore, two crystal plates with high diffraction efficiency at nearly normal incidence are required for X-ray FPR experiments. For sapphire crystals we choose (0 0 0 30) as the backward reflection, and the incident photon energy to fulfill the Bragg condition has to be 14.3147 keV. For simplicity, the notation $T_1/d_g/T_2$ is used to denote the FPR size.

In order to design a FPR with a reasonable efficiency, numerical calculations of the transmittance of the resonator are performed using the dynamical diffraction theory for a Cartesian coordinate system (Stetsko & Chang, 1997) and the recursion relations for X-ray diffracted waves in a layered crystal system (Kohn *et al.*, 2000).

The calculation starts with the fundamental equation of the wavefield to obtain the allowed propagating modes of the electromagnetic waves (EM waves) inside the crystal. The continuities of EM fields on the crystal boundaries are employed to match and determine the EM waves inside and outside the crystal. The diffracted, transmitted, backward-diffracted and backward-transmitted amplitudes, $r(d)$, $t(d)$, $\bar{r}(d)$ and $\bar{t}(d)$, respectively, are related to the resultant EM waves, where d is the thickness of the crystal and the overlines denote amplitudes under the rear surface incident geometry.

In the case of FPRs, a regular FPR consisting of two crystal plates can be treated as a three-layer system that is composed of two crystal plates divided by a vacuum layer. The diffractive and transmitted amplitudes of each layer are calculated by the dynamical diffraction theory, denoted as $r_i(d_i)$, $t_i(d_i)$, $\bar{r}_i(d_i)$ and $\bar{t}_i(d_i)$, respectively, where the subscripts are the layer indices. The effective diffractive and transmitted amplitudes of the layered system are derived from the recurrence formulae (Kohn *et al.*, 2000), which are

$$R_{1:i+1} = R_{1:i} + \frac{\overline{T}_{1:i} r_{i+1} T_{1:i}}{1 - r_{i+1}\overline{R}_{1:i}}, \quad (1)$$

$$T_{1:i+1} = \frac{t_{i+1} T_{1:i}}{1 - r_{i+1}\overline{R}_{1:i}}, \quad (2)$$

$$\overline{R}_{1:i+1} = \bar{r}_{i+1} + \frac{t_{i+1}\overline{R}_{1:i}\bar{t}_{i+1}}{1 - r_{i+1}\overline{R}_{1:i}}, \quad (3)$$

$$\overline{T}_{1:i+1} = \frac{\bar{t}_{i+1}\overline{T}_{1:i}}{1 - r_{i+1}\overline{R}_{1:i}}, \quad (4)$$

where the subscripts $1{:}i$ denote that the considered crystal layers are from the 1st to the ith layer. Hence, the effective reflectivity and transmittance spectra of FPRs can be obtained.

The simulated transmittance spectrum of (0 0 0 30) from a 40/90/40 sapphire FPR at 14.3147 keV is shown in Fig. 3(*a*) as the red solid curve, where the two crystal plates, each of thickness 40 µm, are separated by a 90 µm gap. The black dashed curve is the spectrum of the backward diffraction from a single-crystal plate with a thickness of 80 µm, which equals the sum of the two crystal thicknesses. Comparing the red solid curve with the black dashed curve in Fig. 3(*a*), the fringes on the red solid curve are the resonance peaks. For optical FPRs, the energy separation of the adjacent peaks, E_f, is the so-called free spectral range that can be estimated by the formula $E_f/\Gamma = (\pi\sqrt{R})/(1-R)$, where Γ is the bandwidth of the resonance peaks and R is the reflectivity of the mirrors used in the FPR. The ratio E_f/Γ indicates the resonance efficiency of the FPR, the so-called finesses, F. E_f also depends on the gap between the two mirrors, d, in a FPR, which is described as $E_f = hc/2d$, where parameters h and c are Planck's constant and the speed of the light, respectively. Likewise, Fig. 3(*b*) shows the spectrum from a 24.4/107/24.8 FPR that matches the real dimensions of the FPR shown in Fig. 4. For hard X-ray resonators, the optical reflections from mirrors are replaced by diffractions from crystals so that the formula to estimate E_f needs to be modified. The analytical estimation of E_f has been derived (Shvyd'ko, 2004) as

$$E_f = hc \bigg/ \left[2d_g \frac{\sin^2\theta}{|\gamma_H|} \left(1 + \frac{2d_e(0)}{d_g} \right) \right], \quad (5)$$

where θ and γ_H denote the incident angle and the direction cosines of the reflection. The $d_e(0)$ term is the extinction length of X-rays in sapphire; specifically, $d_e(0)$ = 16 µm for Al_2O_3(0 0 0 30) at 14.3147 keV. Following equation (5), E_f of

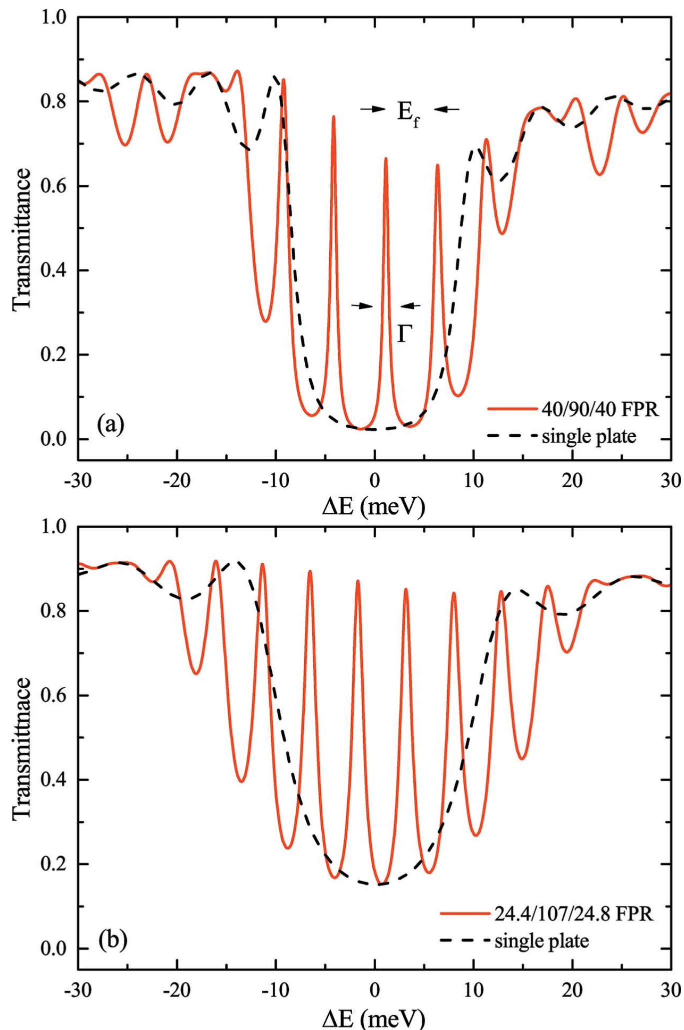

Figure 3
Simulated transmittance spectra of the (0 0 0 30) from (*a*) a 40/90/40 sapphire FPR, (*b*) a 24.4/107/24.8 sapphire FPR. The black dashed curves are the calculated spectra of corresponding single-crystal plates at 14.3147 keV.

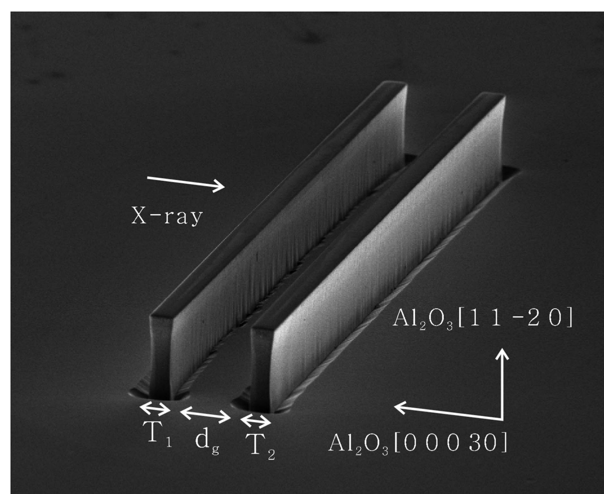

Figure 4
SEM image of a sapphire hard X-ray FPR that is designed with a 40/90/40 geometry (*i.e.* the two plates are each 40 µm thick, separated by a 90 µm gap). The crystal orientations are also denoted on the image.

the 40/90/40 sapphire FPR is around 5.08 meV. Here we ignore the mis-orientations between the crystal surfaces and the atom planes (the so-called miscut) and only consider the nearly normal incident geometry, meaning $\sin\theta \simeq 1$ and $\gamma_H \simeq -1$.

The sapphire FPRs are fabricated by the ICP etching technique (Chen *et al.*, 2015) on 2-inch sapphire wafers of thickness 325 µm that were grown using the heat exchanger method. The shapes and the dimensions of the resultant microstructures are revealed by scanning electron microscopy (SEM) (see Fig. 4). The orientations shown in Fig. 4 indicate that $Al_2O_3[1\,1\,\bar{2}\,0]$ and $Al_2O_3[0\,0\,0\,30]$ are parallel to and perpendicular to, respectively, the surface normal of the wafers. The miscuts along the $Al_2O_3[1\,1\,\bar{2}\,0]$ and $Al_2O_3[0\,0\,0\,30]$ directions are around 0.01° and 0.1°, respectively; these are small enough to be safely ignored. Each crystal plate is designed with the dimensions 1000 µm width, 100 µm height and 40 µm thickness, and the gap between the two plates is 90 µm.

2.3. Synchrotron diffraction experiments

In order to observe the resonance spectra of FPRs, the energy scan method, which involves tuning the energy of the incident beam, is employed. The energy resolution, ΔE, of the incident beam should be narrower than E_f and Γ to avoid blurring of the spectral characteristics. The energy resolution ΔE also relates to the longitudinal coherence length L_c described by the formula $L_c \simeq hc/(2\Delta E)$. L_c should be longer than $2d_g$ to ensure that the beams interact coherently inside the FPRs. The use of a four-bounce high-resolution monochromator (HRM) to improve the energy resolution is essential for the spectral measurements of FPRs.

The spectral measurement of sapphire FPRs experiments were carried out at the Taiwan undulator beamline BL12XU at the SPring-8 synchrotron radiation facility in Japan. The permanent monochromator at BL12XU, a Si(111) DCM, with an energy resolution around 2 eV at 14.3147 keV, is insufficient to observe the resonance fringes. Hence, we have designed and constructed an extremely asymmetrically cut four-bounce HRM based on the design reported (Yabashi *et al.*, 2001). The specifications of the HRM used for the sapphire FPR experiments are listed in Table 1.

At 14.3147 keV, the designed performance of the four-bounce HRM are as follows: the acceptance angle is 13.08 µrad, the spread angle is 9.64 µrad, the vertical magnification of the beam size is 0.50 and energy resolution is 0.30 meV. The cut-off energy of this arrangement is approximately 14.3447 keV.

The experimental setup is illustrated in Fig. 5. The HRM is located after the DCM to improve the energy resolution and to compress the vertical beam size. The X-ray beam size is limited and compressed by the slits and the HRM to 60 µm in the vertical and 200 µm in the horizontal directions on the FPR. The FPR is placed at the center of an eight-circle diffractometer manufactured by Huber. The transmitted resonant photons are detected by an avalanche photodiode (APD) system produced by FMB Oxford. In front of the APD, a set of slits of size 20 µm in the vertical and 100 µm in the horizontal directions block diffused photons and confine the detecting area to improve contrast and the signal-to-noise ratio.

Table 1
Design parameters of the HRM used for the experimental measurements of the sapphire FPRs.

	Crystal 1	Crystal 2	Crystal 3	Crystal 4
Diffraction	Si(4 2 2)	Si(4 2 2)	Si(11 5 3)	Si(11 5 3)
Miscut (°)	15.87	20.93	82.05	82.05
Bragg angle (°)	23.00	23.00	83.10	83.10
Grazing angle (°)	7.13	2.07	1.05	1.05

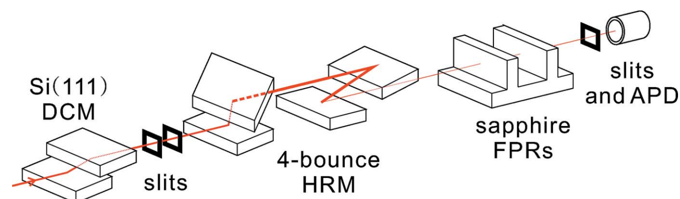

Figure 5
Experimental setup for the spectral measurements with FPRs.

Fig. 6 shows the measured resonance spectra of the designed 40/90/40 FPRs on the two kinds of sapphire wafers: the HEM sapphire FPR shown in red and the KYM sapphire FPR in blue. The observed characteristics are similar to the simulation in Fig. 3(*a*). However, the observed E_f is 4.41 meV rather than the predicted value of 5.08 meV. The measured results are not completely equivalent to the simulated spectrum, and the spectral efficiency and the contrast of these two FPRs are quite different from each other.

Crystal shape distortions and defects in the sapphire crystals indeed cause the differences in FPR performance. Fig. 7(*a*) shows the shape distortions recorded by a SEM photograph of the 40/90/40 sapphire FPR; Fig. 7(*b*) gives quantified distortion values of Fig. 7(*a*). The measuring interval was 20 µm in the vertical direction, where the thicknesses and the corre-

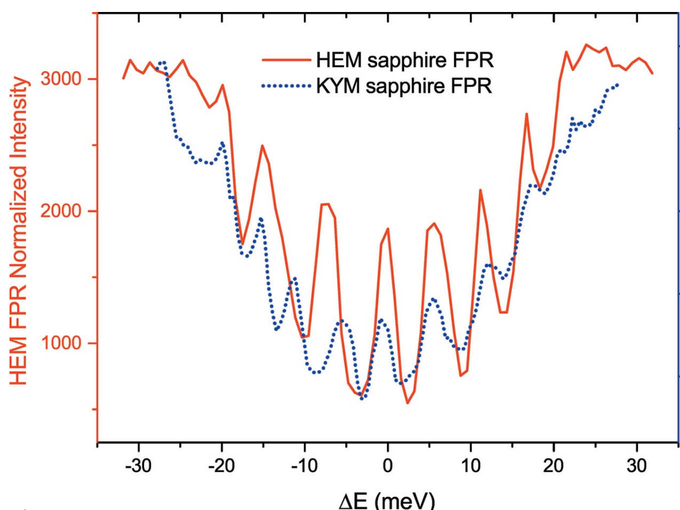

Figure 6
Measured resonance spectra of the HEM and the KYM FPRs that were designed with 40/90/40 µm geometries.

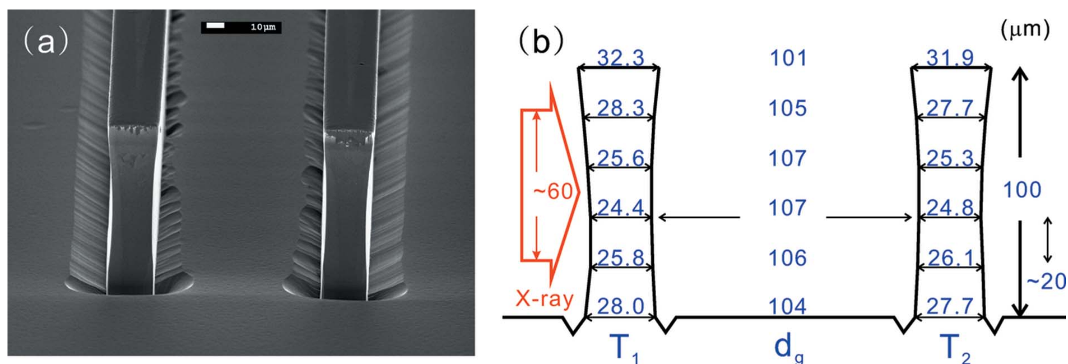

Figure 7
(*a*) SEM image and (*b*) estimated dimensions of the 40/90/40 sapphire FPR. The number columns indicate the estimated thicknesses and gaps at different heights from (*a*).

sponding gaps are indicated. Those results will be discussed later.

3. Discussions

For the spectral measurements, it is obvious that the measured free spectrum range, 4.41 meV, is significantly different from the predicted value of 5.08 meV. In order to explain this difference, we have examined the accuracy of the shape of the crystal plates and the size of the gap by SEM, and we have studied the crystal qualities using X-ray topography.

In Fig. 7(*a*), ideally the side-walls of the crystal plates should be flat and vertical, but in practice they are curved. In reality, the sapphire FPR that was designed to be 40/90/40 had actual dimensions of 24.4/107/24.8, the simulation spectrum of which is shown in Fig. 3(*b*). Based on the measured size of the gaps, Table 2 lists the corresponding E_f estimations which are from 4.53 to 4.46 meV, in contrast to the measured E_f of 4.41 meV, that implies the effective gap size is slightly wider than 107 μm.

Conventionally, the sensitivity of the resonance phenomena of FPRs depends on the wavelength, which is in the sub-Å range for hard X-ray studies. Hence, the surface roughness and the manufacturing accuracy are always serious issues for hard X-ray optical devices. The concept of round trip phase is a convenient way to quantify the issues of dimensional accuracy in the spectral measurements of FPRs (Tsai *et al.*, 2015).

Table 2
Gaps and corresponding predicted E_f compared with the experimental result.

Gap (μm)	105	106	107	Measured
E_f (meV)	4.53	4.49	4.46	4.41

Whenever the beam is injected into the gap of a FPR, the beam is diffracted and trapped between the two diffractive crystal plates, as illustrated in Fig. 8(*a*). The amplitude after a round trip is

$$\exp\big[-i(-n_g K\hat{z})\cdot(-d_g\hat{z})\big]\mathcal{R}_2\exp\big[-i(n_g K\hat{z})\cdot(d_g\hat{z})\big]\overline{\mathcal{R}}_1 = C\exp(i\varphi_r), \qquad (6)$$

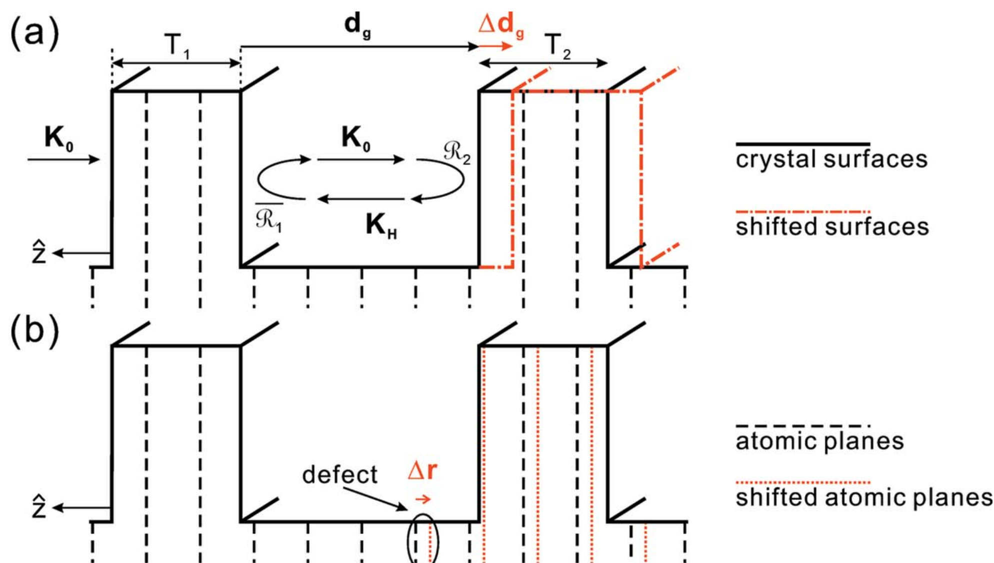

Figure 8
Schematic diagram of crystal FPRs for hard X-rays, showing (*a*) dimensional errors $\Delta\mathbf{d}_g$ and (*b*) dislocations $\Delta\mathbf{r}$.

including propagating and diffractive terms. Here we assume that the beam arrives at nearly normal incidence, and ignore the miscut effect. This means that the beams propagate with wavevectors $\mathbf{K}_0 = -\mathbf{K}_\mathbf{H} = -K\hat{z}$, where n_g is the refractive index of the material filled in the gap, and K, which is equal to $2\pi/\lambda$, is the wavenumber of the incident beam with wavelength λ in a vacuum. The $\mathcal{R}_i$ terms in the form $|\mathcal{R}_i|\exp(i\varphi_i)$ are the amplitudes of the beams diffracted by crystal plates (the overline implies the rear surface incident geometry). The relationships among $\mathcal{R}_i$ differ significantly between the case of optical mirrors and the case of diffractive crystal plates. The $\mathcal{R}_i$ terms in optics depend on the mirrors used, but in X-ray diffraction they not only depend on the chosen diffractions but also change with the diffractive geometries and the periodic susceptibility inside the crystals.

Considering the illustration in Fig. 8(*a*), the front surface of the first crystal plate is placed at $z = 0$ with thickness T_1. Referring to the dynamical theory of X-ray diffraction, the diffraction amplitude of the first crystal is defined as $\mathcal{R}_1 = |\mathcal{R}_1|\exp(i\varphi_1)$; here φ_1 is approximately $-\pi/2$ near the Bragg condition. As the front surface of the second crystal plate is placed at $z = -(T_1 + d_g)$, the reflection amplitude is $\mathcal{R}_2 = \exp[-i\mathbf{H}\cdot(-T_1\hat{z} - d_g\hat{z})]\mathcal{R}_1$. Here the exponential term introducing phase shift $\exp(-i\mathbf{H}\cdot\mathbf{r})$ is due to the continuity of the susceptibility along $\mathbf{H}$ inside the crystal, where $\mathbf{H}$ is the reciprocal lattice vector of the present diffraction, because the single-crystal FPRs are fabricated monolithically; $\mathbf{r}$ indicates the location of the diffractive surface related to $z = 0$. Similarly, in the rear surface incident geometry, $\overline{\mathcal{R}}_1 = \chi_{\overline{\mathbf{H}}}/\chi_\mathbf{H}\exp[\overline{\mathbf{H}}\cdot(-T_1\hat{z})]$, where $\overline{\mathbf{H}} = -\mathbf{H}$ along the z axis, $\chi_\mathbf{H}$ and $\chi_{\overline{\mathbf{H}}}$ are the corresponding susceptibilities of the $\mathbf{H}$ and $\overline{\mathbf{H}}$ diffractions, and $\chi_{\overline{\mathbf{H}}}/\chi_\mathbf{H} = 1$. Nearly the backward diffraction condition, $\mathbf{H}$ approximates to $2n_\mathbf{H}K\hat{z}$, where $n_\mathbf{H}$ is the effective refractive index inside the crystal. In a brief conclusion, whenever the injected X-ray beam undergoes a round trip in the gap, the phase difference of the wavefields is

$$\varphi_r = -2n_gKd_g - \pi + 2n_\mathbf{H}Kd_g = 2Kd_g(n_\mathbf{H} - n_g) - \pi. \quad (7)$$

If the position of the front surface of the second crystal plate deviates from $z = -(T_1 + d_g)$ to $-(T_1 + d_g + \Delta d_g)$, as illustrated in Fig. 8(*a*), the induced phase error is $\Delta\varphi_r = 4\pi/\lambda\Delta d_g(n_\mathbf{H} - n_g)$. The $n_\mathbf{H} - n_g$ term is -3.98×10^{-6} for the sapphire FPRs, where $n_g = 1$ is the refractive index for a vacuum; this sets the tolerance limit for the manufacturing accuracy of hard X-ray FPRs. According to the observations in Fig. 7(*b*), the gap size variations are over 2 µm in the area of the incident X-ray beam (around 60 µm in the vertical direction) illuminating the FPR. The dimensional deviations over 2 µm induce phase shifts over $-\pi$ that cause blurs and distortions on the observed resonance spectra.

Additionally, the crystal quality also influences the resultant spectra. In the previous discussion, the continuity of the susceptibility justified using the shift factor $\exp(-i\mathbf{H}\cdot\mathbf{r})$ to estimate the tolerance of the surface roughness. However, if defects such as dislocations or stacking faults are present, the continuity is broken, which is illustrated in Fig. 8(*b*). Hence, an additional phase shift occurs that can be described by $\exp(-i\mathbf{H}\cdot\Delta\mathbf{r})$, where $\Delta\mathbf{r}$ is the displacement vector caused by defects. Compared with the phase shift due to position deviation Δd_g, the phase shift due to defects changes rapidly, because $1/|\mathbf{H}|$ and $\Delta\mathbf{r}$ are usually comparable in magnitude. In our experiments, the resonance characteristics would be washed out if the X-rays illuminated an area on the FPR that included more than one domain.

Also, the topographic image, Fig. 2(*b*), of the HEM sapphire wafer indicates that only the clear areas containing single-crystal domains are satisfactory for the manufacture of FPRs. The topographic results agree with the spectral measurements of FPRs in Fig. 6, in that the resonance phenomena are more obvious in the HEM sapphire FPR than in the KYM one. These SEM and topographic results also confirm the reasons for the differences between the measured and designed resonance spectra.

4. Conclusions

In order to enhance the efficiency of hard X-ray FPRs, sapphire wafers were used. Compared with the previously developed silicon FPRs, sapphire FPRs not only have a lower absorption coefficient but also the intrinsic property of avoiding multi-beam diffraction effects, which decrease the energy losses in FPRs. The thickness of the crystal plates and the gap of the sapphire FPRs were designed to be 40 µm and 90 µm, respectively, and Al_2O_3(0 0 0 30) was employed for backward diffraction at 14.3147 keV. The resonance spectra of the sapphire FPRs were observed and recorded. It was found that the calculated and the measured spectra had similar characteristics but did not completely match in detail; consequently, SEM and X-ray topographic measurements were performed to determine the cause of the deviations. The SEM images indicated that the side-wall of the crystal plates comprising the FPRs were curved, which influenced the dimensions of the thicknesses and the gap. The FPRs that had been designed to be 40/90/40 were in fact 24.4/107/24.8 FPRs; when this discrepancy was accounted for, the corresponding spectral simulation agreed with the observed spectra. The crystal quality of the sapphire wafers was also verified. The topographic results provided information about the defect density of the two kinds of sapphire wafers that were used in this study. The HEM sapphire wafers were found to be useful for the fabrication of sapphire FPRs, but the Kyropoulos sapphire wafers were not. This conclusion has also been confirmed in spectral experiments where the resonance fringes from the HEM sapphire FPR are more obvious than those from the Kyropoulos sapphire FPR. Additionally, the effects of defects, dimensional inaccuracies and the curved surface of crystal plates were discussed and analyzed. We have not only successfully fabricated prototypes of sapphire FPRs but have also investigated sapphire FPRs in detail. These sapphire FPRs will be able to serve as high-efficiency resonance devices in hard X-ray optics. Moreover, the resonance fringes of FPRs, which are narrow and sequential peaks on the spectra, could be employed as monochromators and analyzers for applications requiring high energy-resolution synchrotron experi-

ments. FPRs also have the potential to provide longitudinal coherent X-ray seeded sources (Amann *et al.*, 2012) in studies of self-seeding free-electron lasers. Comparing the performances of FPRs and high-resolution monochromators, the use of FPRs not only improves the energy resolution to several sub-meV but reduces the timing delay of X-ray seeding due to the geometrical extension of light paths through HRMs from tens of microseconds to hundreds of femtoseconds because the dimensions of FPRs are typically in the sub-millimeter range.

Acknowledgements

The authors are indebted to the Ministry of Science and Technology and Ministry of Education for financial support. The technical assistance from the NSRRC and SPring-8 is also gratefully acknowledged.

References

Amann, J., Berg, W., Blank, V., Decker, F.-J., Ding, Y., Emma, P., Feng, Y., Frisch, J., Fritz, D., Hastings, J., Huang, Z., Krzywinski, J., Lindberg, R., Loos, H., Lutman, A., Nuhn, H.-D., Ratner, D., Rzepiela, J., Shu, D., Shvyd'ko, Y., Spampinati, S., Stoupin, S., Terentyev, S., Trakhtenberg, E., Walz, D., Welch, J., Wu, J., Zholents, A. & Zhu, D. (2012). *Nat. Photon.* **6**, 693.

Chang, S.-L., Stetsko, Y. P., Tang, M.-T., Lee, Y.-R., Sun, W.-H., Yabashi, M. & Ishikawa, T. (2005). *Phys. Rev. Lett.* **94**, 174801.

Chang, Y.-Y., Chen, S.-Y., Wu, H.-H., Weng, S.-C., Chu, C.-H., Lee, Y.-R., Tang, M.-T., Stetsko, Y., Shew, B.-Y., Yabashi, M. & Chang, S.-L. (2010). *Opt. Express*, **18**, 7892.

Chen, P.-C., Lin, P.-T., Mikolas, D. G., Tsai, Y.-W., Wang, Y.-L., Fu, C.-C. & Chang, S.-L. (2015). *J. Micromech. Microeng.* **25**, 015016.

Chen, W. M., McNally, P. J., Shvyd'ko, Y. V., Tuomi, T., Danilewsky, A. N. & Lerche, M. (2003). *J. Cryst. Growth*, **252**, 113–119.

Dash, W. C. (1959). *J. Appl. Phys.* **30**, 459.

Khattak, C. P. & Schmid, F. (2001). *J. Cryst. Growth*, **225**, 572–579.

Kohn, V. G., Shvydko, Y. V. & Gerdau, E. (2000). *Phys. Status Solidi B*, **221**, 597–615.

Shvyd'ko, Y. (2004). *X-ray Optics: High-Energy-Resolution Applications.* Berlin: Springer.

Shvyd'ko, Y. V. & Gerdau, E. (1999). *Hyperfine Interact.* **123**/**124**, 741–776.

Shvyd'ko, Y. V., Lerche, M., Wille, H.-C., Gerdau, E., Lucht, M., Rüter, H. D., Alp, E. E. & Khachatryan, R. (2003). *Phys. Rev. Lett.* **90**, 013904.

Shvyd'ko, Y., Stoupin, S., Blank, V. & Terentyev, S. (2011). *Nat. Photon.* **5**, 539.

Stetsko, Yu. P. & Chang, S.-L. (1997). *Acta Cryst.* A**53**, 28–34.

Sutter, J. P., Alp, E. E., Hu, M. Y., Lee, P. L., Sinn, H., Sturhahn, W., Toellner, T. S., Bortel, G. & Colella, R. (2001). *Phys. Rev. B*, **63**, 094111.

Tsai, Y.-W., Chang, Y.-Y., Wu, Y.-H., Liu, W.-C., Peng, C.-C., Hsieh, W.-F. & Chang, S.-L. (2015). *Opt. Lett.* **40**, 2969–2972.

Wu, Y.-H., Tsai, Y.-W., Chu, C.-H., Liu, W.-C., Chang, Y.-Y. & Chang, S.-L. (2015). *Opt. Express*, **23**, 232934.

Yabashi, M., Tamasaku, K., Kikuta, S. & Ishikawa, T. (2001). *Rev. Sci. Instrum.* **72**, 4080.